Received 17 January 2025; revised 9 April 2025; accepted 13 May 2025.
Date of publication 22 May 2025; date of current version 2 June 2025.

Digital Object Identifier 10.1109/OAJPE.2025.3572769

Efficient, Robust, and Comprehensive Fault Calculation of IBR-Rich Systems Considering Diverse Controls

XINQUAN CHEN[1] (Graduate Student Member, IEEE), ABOUTALEB HADDADI[2] (Senior Member, IEEE), ZHE YANG[3] (Member, IEEE), EVANGELOS FARANTATOS[2] (Senior Member, IEEE), AND ILHAN KOCAR[4] (Senior Member, IEEE)

[1]Department of Electrical and Electronic Engineering, The Hong Kong Polytechnic University, Hong Kong, SAR, China
[2]Electric Power Research Institute (EPRI), Palo Alto, CA 94301 USA
[3]Department of Electrical and Electronic Engineering, Imperial College London, SW7 2AZ London, U.K.
[4]Polytechnique Montréal, Montreal, QC H3T 1J4, Canada

CORRESPONDING AUTHOR: Z. YANG (zhe.yang@imperial.ac.uk)

This work was supported in part by The Hong Kong Polytechnic University (PolyU) Presidential Ph.D. Fellowship Scheme and Hong Kong Research Grant Council for Research Project under Grant 15229421.

ABSTRACT This paper proposes a comprehensive, robust and efficient solver platform that incorporates phasor domain short circuit models of grid-forming (GFM) and grid-following (GFL) IBRs for fundamental frequency fault calculations considering various IBR controls. The proposed approach is verified through cross examination against detailed electromagnetic transient (EMT) modeling and simulations using a modified IEEE 39 bus system with multiple IBRs. The solver platform enables protection engineers to perform rapid and accurate short-circuit computations and protective relay studies in power systems with high penetration of IBRs, facilitating the assessment of fault-ride-through strategies and compliance with grid codes. This paper integrates a recently proposed derivative solution into modified augmented nodal analysis (MANA) formulation for improved numerical convergence under IBRs while treating both GFL and GFM IBR models to provide new insights and results.

INDEX TERMS Current limiter, fault ride-through, inverter-based resources, short circuit calculation, protective relaying.

I. INTRODUCTION

THE inverter-based resources (IBRs) in power systems are increasing, facilitating renewable energy sources adoption, particularly wind [1], [2]. IBRs can be classified into grid-following IBRs (GFL-IBRs) and grid-forming IBRs (GFM-IBRs) based on their converter control strategies [3]. GFL-IBRs mainly act as a power-regulated current source with limited frequency and voltage support capability. By contrast, GFM IBRs can provide full voltage and frequency support services needed for stable grid operation without relying on traditional synchronous generators (SGs). GFM-IBRs demonstrate superior frequency and voltage stability, especially in weak grid connections [4].

During fault ride-through (FRT) mode, IBRs must comply with current injection requirements specified by grid codes [5]. This necessitates efficient evaluation of FRT strategy performance by analyzing IBR current and voltage phasors across various fault scenarios to verify compliance with interconnection requirements. GFM-IBRs exhibit distinct fault behavior compared to GFL-IBRs and synchronous generators (SGs) [6], which varies further when adapted to meet grid codes [7]. Asymmetrical faults introduce sequence components that affect IBR positive and negative sequence component regulation, creating challenges in FRT control design, short-circuit analysis, and protective relaying studies [8]. Recent grid codes specifically require IBRs to provide additional positive and negative sequence reactive current through FRT strategies [9] to enhance low-voltage ride-through (LVRT) capability [10], [11]. This can be achieved using current limiters within a

positive and negative sequence control (PNSC) framework [12], [13].

Current limiter selection in FRT strategies requires careful consideration [14]. Common types include current saturation-based (CS-based) and virtual impedance-based (VI-based) limiters [15]. CS-based limiters, comprising instantaneous [16], magnitude [17], and priority-based [18] variants, are applicable in both GFL-IBRs and GFM-IBRs. Under FRT mode, CS-based limiters specify *dq* current references in the PNSC structure, allowing IBRs to function as current injection sources in short-circuit networks.

VI-based limiters enable GFM-IBRs to maintain voltage source characteristics while restricting converter currents during faults by modifying terminal voltage references through virtual impedance control [19]. When implemented in the positive sequence loop, GFM-IBRs can be modeled as a voltage source with virtual impedance [20]. To emulate SG behavior, GFM-IBRs can function as current sources in the negative sequence system [21]. These controls, implemented within PNSC structure, allow GFM-IBRs to mirror SG behavior under fault conditions.

Accurate short-circuit modeling for IBRs with various FRT strategies is crucial for future IBR-rich systems. While detailed electromagnetic transient (EMT) models exist [13], [22], their computational intensity limits efficiency across multiple fault scenarios. Research has produced simplified models to improve analysis efficiency: For GFL-IBRs, phasor domain models incorporating FRT strategies have been developed for Type-III [23], [24] and Type-IV [25] wind turbines. The analysis employs modified augmented nodal analysis (MANA) with fixed-point solver [26], [27]. Fixed-point methods exhibit several limitations for power system applications: high sensitivity to parameter selection and initial conditions; poor convergence characteristics for large-scale or complex networks; inferior robustness compared to derivative-based approaches; and susceptibility to divergence when applied to problems with significant nonlinearities or discontinuities that disrupt the iterative solution process. To overcome these issues, this paper integrates the Newton-based approach of [28] and [29] into MANA formulation for improved numerical convergence under IBRs.

Recent research has produced various GFM models: RMS models under synchronous reference frame [30], equivalent models covering transient and steady-state responses [31] positive and negative sequence equivalent circuits [32] implemented in OpenDSS [33], and positive sequence and per-phase phasor models [34], [35]. However, these models generally lack consideration of decoupled-sequence FRT strategies.

This paper focuses on numerical methods for phasor domain analysis, which are utilized by commercial fault analysis programs at an industrial scale. The fault calculation is based on fundamental frequency phasors. Key contributions include:

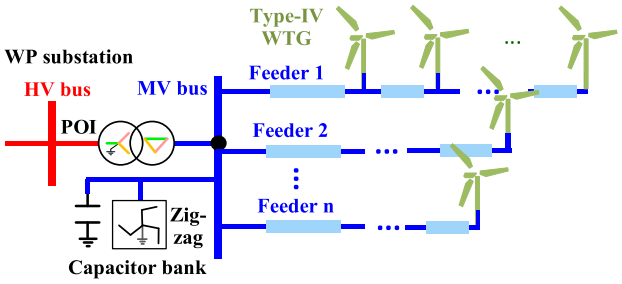

FIGURE 1. **Diagram of a full-size-type IBR plant.**

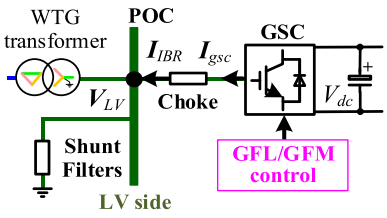

FIGURE 2. **Topology of IBR unit.**

- Proposing fundamental-frequency IBR short-circuit models with various FRT strategies, GFM/GFL controls, and current limiters
- Proposing a comprehensive solver with Newton-based MANA formulation incorporating static IBR models with diverse controls
- Using a large-scale IBR-rich system to demonstrate scalability and new insights for future high-IBR grids

The paper is organized as follows: Section II presents IBR phasor domain short circuit models; Section III details the short circuit solver; Section IV provides validation and comparative studies; and Section V presents conclusions.

II. PHASOR DOMAIN SHORT-CIRCUIT MODEL FOR IBRS CONSIDERING FAULT RIDE-THROUGH CONTROL STRATEGIES

A. BASIC TOPOLOGY AND PNSC STRUCTURE OF GFL- AND GFM-IBR

Fig. 1 shows a typical full-size-type IBR plant, where the power generated by the IBRs is transmitted to the point of interconnection (POI) via a medium-voltage (MV) collector grid, a main IBR transformer, and a high-voltage (HV) bus. In this paper, superscript * denotes the reference. Subscripts + and – denote positive and negative sequences, respectively. Fig. 2 shows the typical topology of a grid-side converter (GSC) of an IBR unit. The choke circuit, shunt filters, and unit transformer are connected at the point of connection (POC) on the low-voltage (LV) side. $\boldsymbol{V}_{LV}$ denotes the LV-side voltage phasor. $\boldsymbol{I}_{IBR}$ denotes the current phasor provided by IBRs. The subscript *gsc* denotes the component on the GSC side.

To ensure stable operation in normal operation, the GFL control typically includes PLL, DC voltage control, AC

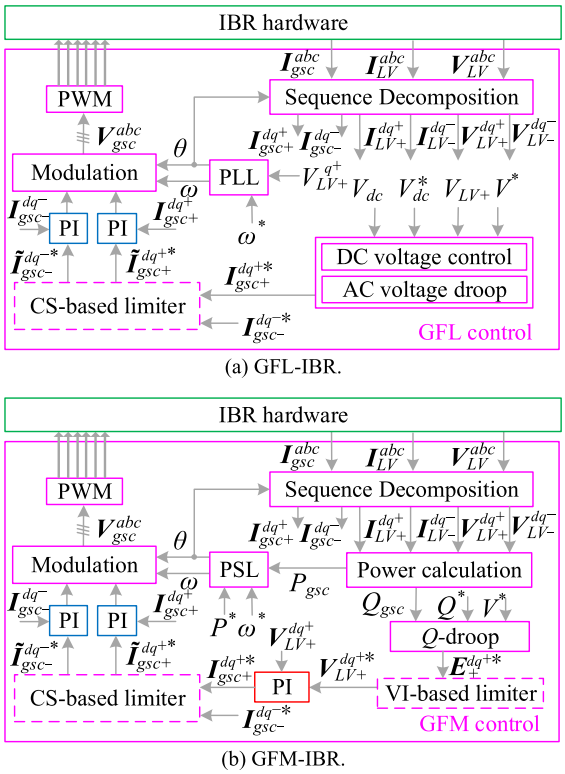

(a) GFL-IBR.

(b) GFM-IBR.

FIGURE 3. PNSC structure for the grid-side converter of IBR.

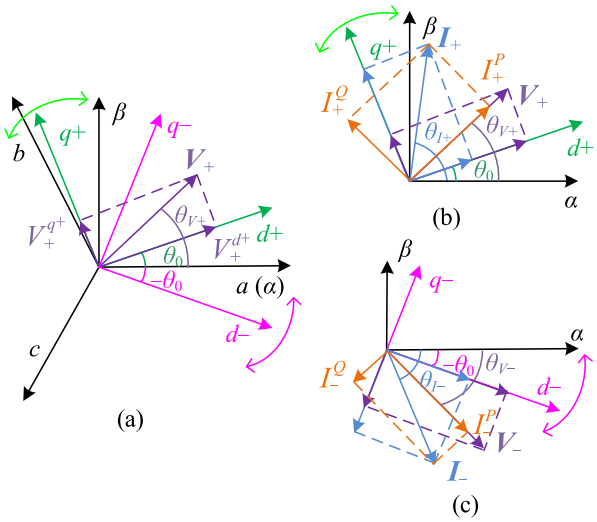

FIGURE 4. Relations between the coordinates for IBR.

voltage droop control, and inner current regulation (blue box) [13], while the GFM control typically incorporates PSL, Q-droop control, inner voltage regulation (red box), and inner current regulation (blue box) [15], as illustrated in Fig. 3. More detailed descriptions of control blocks can be found in [13] and [15]. The PNSC structure aims to appropriately regulate both positive and negative sequence components to comply with current capability and current injection requirements per grid codes.

In this paper, $\{\theta, \omega\}$ denotes the orientation angle and angular frequency. $\{P, Q\}$ denotes the active and reactive powers. Under unbalanced grid conditions, since the zero-sequence components on the grid side are usually separated by a delta-connected IBR transformer, the instantaneous *abc* vectors of IBR can be transformed into $dq+$ and $dq-$ vectors. Superscript $dq+$ denotes components in the $dq+$ coordinate that rotates at the nominal frequency ω_n. Superscript $dq-$ denotes components in the $dq-$ frame that rotates at the nominal frequency $-\omega_n$. Fig. 4(a) illustrates the angular relations between $\boldsymbol{V}_+$ and coordinates. Fig. 4(b) illustrates the phasor representation of positive sequence active and reactive current (I1A and I1R). Fig. 4(c) illustrates the phasor representation of negative sequence active and reactive current (I2A and I2R). These current phasors are given by:

$$\begin{cases} I_+^P + jI_+^Q = I_+ e^{j(\theta_{I+} - \theta_{V+})} \\ I_-^P + jI_-^Q = I_- e^{j(\theta_{I-} - \theta_{V-})} \end{cases} \tag{1}$$

where $\{I_+^P, I_-^P\}$ denotes I1A and I2A. $\{I_+^Q, I_-^Q\}$ denotes I1R and I2R. In Fig. 4, θ_0 denotes the power angle of IBR, which is frozen in FRT mode for the purpose of short-circuit calculation. For clarity, positive and negative sequence voltages are abbreviated as V1 and V2. Positive and negative sequence currents are abbreviated as I1 and I2.

B. CURRENT INJECTION OF IBR UNDER FRT MODE

Under unbalanced grid conditions, I1R is regulated to support V1 and I2R to reduce V2. By using a K-factor-based method [36], the incremental reactive currents are determined by the variation of V1 and V2 as follows:

$$\begin{cases} \Delta I_{gsc+}^{Q*} = K_+^Q \Delta V_{LV+} = K_+^Q (V^* - V_{LV+}) \\ \Delta I_{gsc-}^{Q*} = K_-^Q \Delta V_{LV-} = K_-^Q V_{LV-} \end{cases} \tag{2}$$

where $\left\{K_+^Q, K_-^Q\right\}$ denotes the K factor for reactive current injection. In normal operation, the inner voltage regulation suppresses V_{LV+}^{q+} to zero. Based on Fig. 5, $I_{gsc+}^{Q} = I_{gsc+}^{q+}$. Therefore, the references of I1R and I2R are determined as

$$\begin{cases} I_{gsc+}^{Q*} = I_{gsc+}^{Qpre} + \Delta I_{gsc+}^{Q*} = I_{gsc+}^{q+pre} + \Delta I_{gsc+}^{Q*} \\ I_{gsc-}^{Q*} = \Delta I_{gsc-}^{Q*} \end{cases} \tag{3}$$

where superscript *pre* denotes the pre-fault value. I_{gsc+}^{Qpre} denotes the pre-fault positive sequence reactive current. I_{gsc+}^{q+pre} denotes the pre-fault $q+$ axis current. In normal operation, $I_{gsc+}^{Qpre} = I_{gsc+}^{q+pre}$ since $\theta_{V+} = \theta_0$.

1) NEGATIVE SEQUENCE

To emulate the negative sequence behavior of SGs, I2 is injected leading V2 by 90°. Hence, I2A can be set to zero to spare the current capacity for I2R injection. Fig. 5 depicts the generation of I2R, where $\tilde{\boldsymbol{I}}^*$ denotes the updated current reference. I^{lim} denotes the current limit. Based on the relations

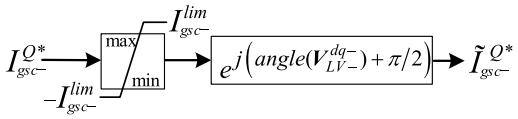

FIGURE 5. Negative sequence current limiter design.

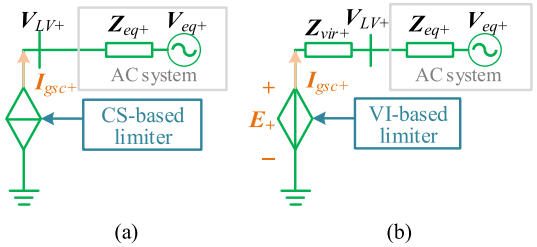

FIGURE 6. Equivalent positive sequence system integrated with IBR under CS-based and VI-based limiters.

in Fig. 4, the $dq-$ current references are derived as

$$\begin{cases} \tilde{I}_{gsc-}^{d-*} = V_{LV-}^{q-}\tilde{I}_{gsc-}^{Q*} \Big/ V_{LV-} \\ \tilde{I}_{gsc-}^{q-*} = -V_{LV-}^{d-}\tilde{I}_{gsc-}^{Q*} \Big/ V_{LV-} \end{cases} \tag{4}$$

2) POSITIVE SEQUENCE

The equivalent positive sequence system integrated with IBR under CS-based and VI-based limiters is shown in Fig. 6, where $\boldsymbol{Z}_{eq+}$ and $\boldsymbol{V}_{eq+}$ denote the equivalent positive sequence impedance and voltage source of AC networks.

Under CS-based limiter, an IBR is equivalent to a current source. Hence, IBR I1 injection is determined by the FRT strategy as a function of the terminal voltage (LV-side voltage phasor) which is retrieved from the iterative solver at each step. The CS-based limiters can be applied to both GFL-IBR and GFM-IBR. For GFL-IBR, due to the regulation of SRF-PLL [2], $V_{LV+}^{q+} = 0$ and $\theta_{V+} = \theta_0$. For GFM-IBR, in the absence of a PLL, $\theta_{V+} \neq \theta_0$. Since the angular relation $(\theta_{V+} - \theta_0)$ of GFM-IBR and GFL-IBR is different, their reaction to I1A and I1R injection will be different. The IEEE 2800 compliant limiter considers this angular relation to address this.

For an IBR under VI-based limiter, the I1 injection is determined by the equivalent voltage source, the virtual impedance of the IBR, and the equivalent network impedance, as given by

$$\boldsymbol{I}_{gsc+} = \frac{\boldsymbol{E}_+ - \boldsymbol{V}_{eq+}}{\boldsymbol{Z}_{vir+} + \boldsymbol{Z}_{eq+}} \tag{5}$$

The VI-based limiter is only implemented in GFM-IBR. These limiters are further elaborated in Section II-C and II-D.

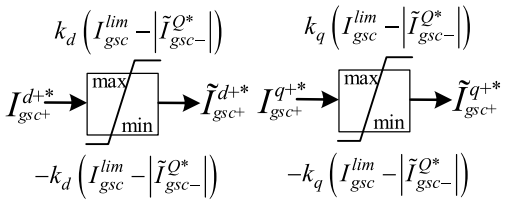

FIGURE 7. Instantaneous current limiter design.

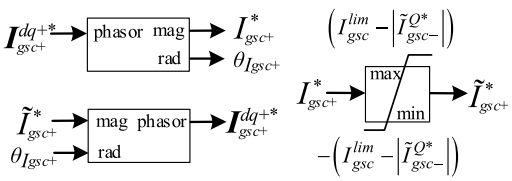

FIGURE 8. Magnitude current limiter design.

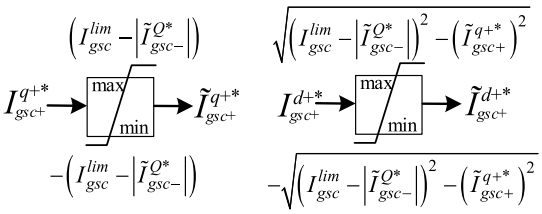

FIGURE 9. Priority-based current limiter design.

C. CURRENT SATURATION-BASED LIMITERS FOR GFL- AND GFM-IBR

Assuming the output active power remains constant during short circuit faults, I_{gsc+}^{d+*} is approximated by

$$I_{gsc+}^{d+*} = \frac{P_{gsc}^{pre}}{V_{LV+}\cos(\theta_{LV+} - \theta_0)} \tag{6}$$

To avoid overcurrent, four types of current limiters are studied and compared in this paper, as below:

1) INSTANTANEOUS LIMITER

The current limiting thresholds are respectively set for $d+$ and $q+$ current references in this type of limiters, as shown in Fig. 7. Hence, the performance is usually conservative, resulting in underuse of the converter's current capacity.

2) MAGNITUDE LIMITER

In this limiter, the magnitude of I1 references is constrained to avoid overcurrent, but its angle would not be affected, as shown in Fig. 8.

3) PRIORITY-BASED LIMITER

This limiter allows the designated priority current to reach the maximum limit. Generally, priority is given to the $q+$ current reference in the FRT mode [13], as shown in Fig. 9.

4) IEEE 2800 COMPLIANT LIMITER

The IEEE 2800 compliant limiter (2800 limiter) is developed to enable IBRs to comply with current injection requirements in the IEEE 2800 standard. With this angular difference $(\theta_{V+}-\theta_0)$, the relations in (1) need to be reconsidered:

$$\begin{cases} I_{gsc+}^{d+*} = I_{gsc+}^{P*}\cos(\theta_{V+}-\theta_0) + I_{gsc+}^{Q*}\sin(\theta_{V+}-\theta_0) \\ = V_{LV+}^{d+}I_{gsc+}^{P*}\Big/V_{LV+} + V_{LV+}^{q+}I_{gsc+}^{Q*}\Big/V_{LV+} \\ I_{gsc+}^{q+*} = I_{gsc+}^{P*}\sin(\theta_{V+}-\theta_0) - I_{gsc+}^{Q*}\cos(\theta_{V+}-\theta_0) \\ = V_{LV+}^{q+}I_{gsc+}^{P*}\Big/V_{LV+} - V_{LV+}^{d+}I_{gsc+}^{Q*}\Big/V_{LV+} \end{cases} \tag{7}$$

Per IEEE 2800 standard, the coordination for I1R and I2R is given by

$$\begin{cases} \Delta I_{gsc+}^{Q*} \geq 0 & \text{During balanced faults} \\ \left|\Delta I_{gsc+}^{Q*}\right| \geq \left|\Delta I_{gsc-}^{Q*}\right| & \text{During unbalanced faults} \end{cases} \tag{8}$$

To ensure that the incremental reactive currents do not exceed the current limit, when $\left|K_+^Q\Delta V_{LV+}\right| + \left|K_-^Q\Delta V_{LV-}\right| > I_{gsc}^{lim}$, the incremental reactive current references are determined as

$$\begin{cases} \left\{\Delta I_{gsc+}^{Q*}, \Delta I_{gsc-}^{Q*}\right\} = \left\{\eta K_+^Q\Delta V_{LV+}, \eta K_-^Q\Delta V_{LV-}\right\} \\ \eta = I_{gsc}^{lim}\Big/\left(\left|K_+^Q\Delta V_{LV+}\right| + \left|K_-^Q\Delta V_{LV-}\right|\right) \end{cases} \tag{9}$$

Combining (2), (3), and (7) yields:

$$\begin{cases} I_{gsc+}^{d+*} = \dfrac{V_{LV+}^{q+}\Delta I_{gsc+}^{Q*}}{V_{LV+}} + \dfrac{P_{gsc}^{pre}}{V_{LV+}\cos(\theta_{LV+}-\theta_0)} \\ I_{gsc+}^{q+*} = -V_{LV+}^{d+}\Delta I_{gsc+}^{Q*}\Big/V_{LV+} + I_{gsc+}^{q+pre} \end{cases} \tag{10}$$

Then the positive sequence limiter in Fig. 9 and negative-sequence limiter in Fig. 5 are employed to avoid overcurrent. Per IEEE 2800 standard, IBRs are expected to fully utilize the maximum current capacity. Hence, a scaling method [36] is employed to ensure that the faulty phase current can reach the current limit, as given by

$$K_{scale} = I_{gsc}^{lim}\Big/\max\left(\left|I_{gsc}^{a*}\right|, \left|I_{gsc}^{b*}\right|, \left|I_{gsc}^{c*}\right|\right) \tag{11}$$

$$\begin{cases} \tilde{\boldsymbol{I}}_{gsc}^{dq+*} = K_{scale}\boldsymbol{I}_{gsc}^{dq+*} \\ \tilde{\boldsymbol{I}}_{gsc}^{dq-*} = K_{scale}\boldsymbol{I}_{gsc}^{dq-*} \end{cases} \tag{12}$$

D. VIRTUAL IMPEDANCE-BASED LIMITER FOR GFM-IBR

For GFM-IBRs, the Q-droop control can be expressed as

$$\begin{cases} E_+^{d+*} = V^* + D_Q(Q^* - Q_{gsc}) \\ E_+^{q+*} = 0 \end{cases} \tag{13}$$

where D_Q denotes control gain. The VI-based limiter restrains fault currents by modifying voltage references:

$$\begin{cases} V_{LV+}^{d+*} = E_+^{d+*} - R_{vir+}I_{gsc+}^{d+*} + X_{vir+}I_{gsc+}^{q+*} \\ V_{LV+}^{q+*} = E_+^{q+*} - R_{vir+}I_{gsc+}^{q+*} - X_{vir+}I_{gsc+}^{d+*} \end{cases} \tag{14}$$

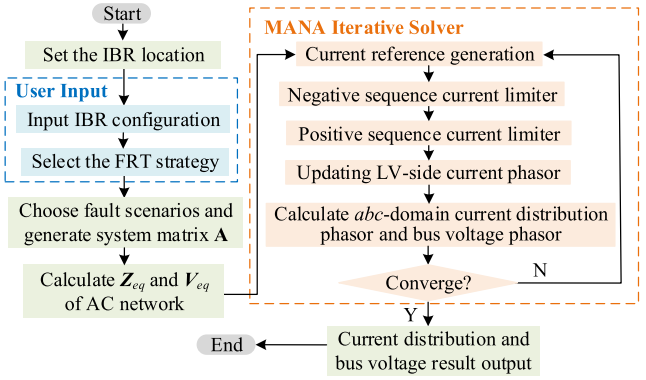

FIGURE 10. Framework of the proposed short-circuit solver.

where $\{R_{vir+}, X_{vir+}\}$ denotes the virtual resistance and reactance. When I_{gsc+} exceeds I_{gsc+}^{lim}, the virtual impedance is given by

$$\boldsymbol{Z}_{vir+} = R_{vir+} + jX_{vir+} = \frac{\Delta V_+(1+j\sigma)}{I_{gsc+}^{lim}\sqrt{1+\sigma^2}} \tag{15}$$

where σ denotes the pre-defined ratio of X_{vir+} over R_{vir+}. ΔV denotes the positive sequence voltage drop across the $\mathbf{Z}_{vir+}$. To ensure I1 reaches I_{gsc+}^{lim} under FRT mode, a PI controller is employed to regulate the current reference tracking the current limit. The details of control loops can be found in [21].

III. SHORT-CIRCUIT SOLVER

A. FRAMEWORK OF SHORT-CIRCUIT SOLVER

The proposed short-circuit solver is illustrated in the framework of Fig. 10.

First, set the IBR location and read user inputs, including IBR configuration and selection of FRT strategies. Fault scenario is selected to generate the system matrix $\mathbf{A}$ that includes the fault represented with switches, then compute sequence domain equivalent impedance ($\boldsymbol{Z}_{eq}$) and equivalent voltage source ($\boldsymbol{V}_{eq}$) of the network as seen from GFM-IBR locations with VI-based limiters. The $\boldsymbol{Z}_{eq}$ and $\boldsymbol{V}_{eq}$ are used to compute I1 injection by (5). For IBRs with CS-based limiters, the current injection is determined by the FRT strategy. Once the phasors I1 and I2 are computed for each IBR, they are converted in the *abc* domain for updating system voltages using the MANA formulation [26], [38].

B. PHASOR DOMAIN SHORT-CIRCUIT MODEL ALGORITHM

The main short-circuit solver algorithm encompasses the following aspects:

1. User Input:

1.1. Input IBR configuration, including:

- IBR parameter: I_{gsc}^{lim}, I_{gsc}^{lim-}, K_+^Q, K_-^Q, D_Q, V^*, Q^*, σ, k_d, k_q.

- Pre-fault value (steady state value in normal operation): θ_0, I_{gsc+}^{q+pre}, and P_{gsc}^{pre}.

1.2. Select the employed FRT strategy or limiter, including: 1-Instantaneous limiter; 2-Magnitude limiter; 3-Priority-based limiter; 4-2800 limiter; 5-VI-based limiter for GFM-IBR only.

2. Short-circuit model algorithm:

2.1. Current reference generation:

IF the employed limiter ==4

Calculate ΔI_{gsc+}^{Q*} and ΔI_{gsc-}^{Q*} by (9);

ELSE

Calculate I_{gsc+}^{Q*} and I_{gsc-}^{Q*} by (2) and (3);

END

Calculate I_{gsc+}^{d+*} by (6).

2.2. Negative sequence current limiter:

IF $I_{gsc-}^{Q*} > I_{gsc-}^{lim}$

$I_{gsc-}^{Q*} = I_{gsc-}^{lim}$;

END

$I_{gsc+}^{lim} = I_{gsc}^{lim} - \left|\tilde{\boldsymbol{I}}_{gsc-}^{Q*}\right|$;

Calculate $\tilde{\boldsymbol{I}}_{gsc-}^{d-*}$ and $\tilde{\boldsymbol{I}}_{gsc-}^{q-*}$ by (4);

$\tilde{\boldsymbol{I}}_{gsc-}^{*} = abs\left(\tilde{\boldsymbol{I}}_{gsc-}^{d-*} + j\tilde{\boldsymbol{I}}_{gsc-}^{q-*}\right) e^{j\left(\theta_0 - angle\left(\tilde{\boldsymbol{I}}_{gsc-}^{d-*} + j\tilde{\boldsymbol{I}}_{gsc-}^{q-*}\right)\right)}$.

2.3. Positive sequence current limiter:

The details of each current limiter are presented in Appendix A. The VI-based limiter is only used in GFM-IBR. The CS-based limiters are applicable to both GFL- and GFM-IBRs. Since the pre-fault values θ_0 and I_{gsc+}^{q+pre} for GFL- and GFM-IBRs differ, their outputs will not be identical even when using the same CS-based limiter.

2.4. Updating LV-side current phasor:

$$\begin{cases} \tilde{\boldsymbol{I}}_{IBR+} = \tilde{\boldsymbol{I}}_{gsc+}^{*} - \boldsymbol{V}_{LV+}/\boldsymbol{Z}_{f+} \\ \tilde{\boldsymbol{I}}_{IBR-} = \tilde{\boldsymbol{I}}_{gsc-}^{*} - \boldsymbol{V}_{LV-}/\boldsymbol{Z}_{f-} \end{cases} \tag{16}$$

where $\{\boldsymbol{Z}_{f+}, \boldsymbol{Z}_{f-}\}$ denotes the phasor domain equivalent impedance of shunt filters.

C. ITERATIVE SOLVER

The proposed short-circuit models can be implemented within a MANA-based iterative solver. For each fault scenario, a sparse system matrix $\mathbf{A}$ is built in the phase domain that can also handle unbalanced distribution systems. The iterative process is described as follows:

Step 1. Compute currents in the sequence domain and transform: The set of $\left\{\tilde{\boldsymbol{I}}_{IBR+}, \tilde{\boldsymbol{I}}_{IBR-}\right\}$ is calculated using the proposed short-circuit models, and transformed into three-phase currents $\tilde{\boldsymbol{I}}_{IBR}$ and populated into $\mathbf{b}$. Hence, $\mathbf{b} = \left[\tilde{\boldsymbol{I}}_{IBR}\boldsymbol{V}_b\mathbf{0}\right]^{\mathrm{T}}$. $\boldsymbol{V}_b$ denotes the known voltage sources in the system.

Step 2. Calculate current distribution phasor and bus voltage phasor**:** Using sparse LU factorization, the equation $\mathbf{Ax} = \mathbf{b}$ is solved to update nodal voltage phasors $\boldsymbol{V}$ and LV-side voltage phasors $\{\boldsymbol{V}_{LV+}, \boldsymbol{V}_{LV-}\}$. The $dq+$ and $dq-$ components of LV-side voltage phasors:

$$\begin{cases} \delta_{V+} = angle(\boldsymbol{V}_{LV+}) - \theta_0 \\ \delta_{V-} = \theta_0 - angle(\boldsymbol{V}_{LV-}) \\ \begin{Bmatrix} V_{LV+}^{d+} & V_{LV+}^{q+} \end{Bmatrix} = abs(\boldsymbol{V}_{LV+}) \begin{Bmatrix} \cos\delta_{V+} & \sin\delta_{V+} \end{Bmatrix} \\ \begin{Bmatrix} V_{LV-}^{d-} & V_{LV-}^{q-} \end{Bmatrix} = abs(\boldsymbol{V}_{LV-}) \begin{Bmatrix} \cos\delta_{V-} & \sin\delta_{V-} \end{Bmatrix} \end{cases} \tag{17}$$

Then go to step 1 for the next iteration until the convergence criterion (18) is satisfied. ε denotes the predefined tolerance for convergence. For the k-th iteration,

$$\begin{cases} \Delta V_{LV+} = abs(\boldsymbol{V}_{LV+}^{(k+1)}) - abs(\boldsymbol{V}_{LV+}^{(k)}) < \varepsilon \\ \Delta V_{LV-} = abs(\boldsymbol{V}_{LV-}^{(k+1)}) - abs(\boldsymbol{V}_{LV-}^{(k)}) < \varepsilon \end{cases} \tag{18}$$

When integrating high-penetration IBRs, the nonlinearity of FRT strategies can compromise the numerical stability of iterative mechanisms, potentially causing non-convergence. To address the challenge, this paper integrates the secant-based variation of Newton's method proposed in [28] into MANA formulation, which represents IBRs by a Norton equivalent in each iteration. The related equations are given in Appendix B for the integrity of paper.

Assuming the Norton admittance in the k-th iteration ($k > 1$) to be given by $\mathbf{Y}_{IBR}^{(k)}$, an additional admittance matrix can be denoted as

$$\mathbf{Y} = \mathrm{diag}\left\{\left[\boldsymbol{Y}_{IBR}^{(k)}\ \mathbf{0}\right]\right\} \tag{19}$$

For the k-th iteration, the system equation $\mathbf{Ax} = \mathbf{b}$ becomes

$$\mathbf{A}\left[\boldsymbol{V}_{LV}^{(k+1)}\ \boldsymbol{I}_m^{(k+1)}\right]^{\mathrm{T}} = \begin{bmatrix} \tilde{\boldsymbol{I}}_{IBR}^{(k)} - \boldsymbol{Y}_{IBR}^{(k)}\left(\boldsymbol{V}_{LV}^{(k+1)} - \boldsymbol{V}_{LV}^{(k)}\right) \\ \boldsymbol{V}_b \\ \mathbf{0} \end{bmatrix} \tag{20}$$

where $\boldsymbol{I}_m$ denotes the current vector of voltage sources, branches, and switches. The basics of MANA formulation can be found in [38].

$$[\mathbf{A} + \mathbf{Y}]\left[\boldsymbol{V}_{LV}^{(k+1)}\ \boldsymbol{I}_m^{(k+1)}\right]^{\mathrm{T}} = \begin{bmatrix} \tilde{\boldsymbol{I}}_{IBR}^{(k)} + \boldsymbol{Y}_{IBR}^{(k)}\boldsymbol{V}_{LV}^{(k)} \\ \boldsymbol{V}_b \\ \mathbf{0} \end{bmatrix} \tag{21}$$

The solver updates node voltage phasors until criterion (18) is satisfied.

IV. IBR SHORT CIRCUIT MODEL AND SOLVER VERIFICATION

A. TEST SYSTEM AND FAULT CASES

In this section, the proposed IBR short-circuit models and solver are verified by comparing the iterative solution with EMT simulation results. The phasor-domain MANA algorithm is implemented in MATLAB R2024a. This code includes a model of the IEEE 39-bus test system, phasor-domain short circuit models of IBRs including both GFL and GFM, and a Newton-Raphson based iterative solver. An EMT version of the IEEE 39-bus system has been developed within

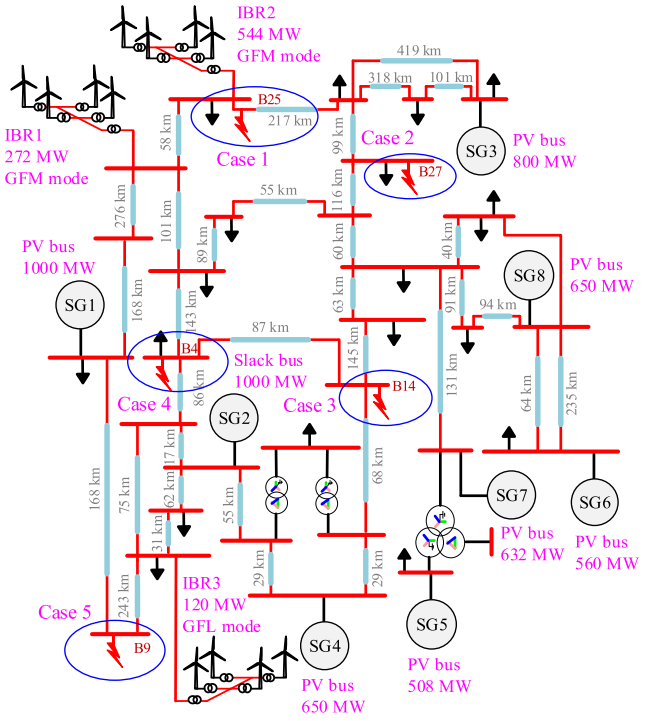

FIGURE 11. Modified IEEE 39 bus system integrated with GFM-IBR and GFL-IBR.

EMTP version 4.3. Reference [40] presents the details of the EMTP model. The IBRs of the EMTP model have been represented by a generic EMT model based on [13]. The test environment consists of a PC with Windows 11 64-bit operating system and an AMD Ryzen 7 7735H processor with Radeon Graphics, featuring 16 CPUs running at 3.2 GHz. A modified 500 kV/60 Hz IEEE 39 bus system integrated with GFM- and GFL-IBRs is used, as shown in Fig. 11. The description of the employed EMT model is presented in Appendix D. Each IBR plant contains an aggregated model of full-size-type IBR units with the PNSC scheme. Droop control is employed as the GFM primary control. The IBR configuration can be found in Table 1. For demonstration purposes, two combination schemes of FRT strategies are set in this system:

Scheme I: IBR1 (GFM mode, magnitude limiter); IBR2 (GFM mode, Instantaneous limiter); IBR3 (GFL mode, priority-based limiter).

Scheme II: IBR1 (GFM mode, 2800 limiter); IBR2 (GFM mode, VI-based limiter); IBR3 (GFL mode, priority-based limiter).

To demonstrate the accuracy and efficiency of the proposed model, three typical fault scenarios are performed, as below:

Case 1: Bolted line-A-to-ground (AG) fault at B25.

Case 2: 10 Ω line-A-to-line-B-to-ground (ABG) fault at B27.

Case 3: 5 Ω line-B-to-line-C (BC) fault at B14.

Case 4: Bolted BC fault at B4.

Case 5: Bolted three-phase-to-ground (ABCG) fault at B9.

TABLE 1. Configurations of IBRs.

Parameter	Value
DC voltage, DC capacitor	1.15 kV, 15 kJ/MVA
Choke impedance, Shunt filter impedance	0.01+0.15j pu, -11.107j pu
I_{gsc-}^{lim}, I_{gsc}^{lim}	0.6 pu, 1.2 pu
Pre-fault I1R	0.022 pu
K factor	3
k_d, k_q	0.5, 0.5
D_Q, σ	0.04, 1

TABLE 2. Phasors of IBR1 under magnitude limiter (Scheme I).

Case	Variable	EMT	Short-circuit Model	Mag. error	Ang. error
1	V_{LVa}	0.553 (17.411°)	0.553 (17.447°)	0.001	-0.04°
	V_{LVb}	0.799 (-87.518°)	0.798 (-87.478°)	0.000	-0.04°
	V_{LVc}	0.846 (131.664°)	0.846 (131.668°)	0.000	0°
	I_{IBRa}	1.067 (-27.526°)	1.065 (-27.352°)	0.002	-0.17°
	I_{IBRb}	0.166 (-139.702°)	0.163 (-138.333°)	0.003	-1.37°
	I_{IBRc}	1.016 (143.759°)	1.018 (144.022°)	-0.002	-0.26°
2	V_{LVa}	0.803 (22.192°)	0.807 (22.027°)	-0.004	0.17°
	V_{LVb}	0.804 (-87.319°)	0.807 (-87.532°)	-0.003	0.21°
	V_{LVc}	0.928 (147.392°)	0.931 (147.225°)	-0.003	0.17°
	I_{IBRa}	1.195 (6.874°)	1.196 (5.902°)	-0.001	0.97°
	I_{IBRb}	0.796 (-124.158°)	0.801 (-125.555°)	-0.005	1.4°
	I_{IBRc}	0.902 (145.112°)	0.897 (143.849°)	0.005	1.26°

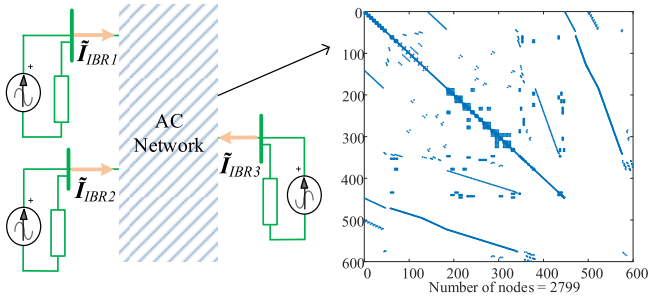

FIGURE 12. Visualized sparsity pattern of matrix A.

In system matrix **A**, the switches can be set to 0 (open) or 1 (closed) for changing fault scenarios, including any type and number of simultaneous shunt or series faults. The sparsity pattern of matrix **A** is shown in Fig. 12.

B. ACCURACY UNDER VARIOUS FRT STRATEGIES

Tables 2–7 present the voltage and current phasors, formatted as "magnitude (angle)". The magnitude is expressed in per unit (pu) and the angle in degrees. The predefined tolerance for convergence is set to 0.0005 pu. In EMT simulation, FRT strategies are activated at the inception of faults and continue to operate without interruption for validation purposes.

The comparison of the iterative solver with EMT simulations shows that the proposed models accurately estimate the current contribution and voltage support capability of multi-IBRs under various FRT strategies. The absolute error is within 0.01 pu in magnitude and 2.1° in angle, caused by

TABLE 3. Phasors of IBR2 under instantaneous limiter (Scheme I).

Case	Variable	EMT	Short-circuit Model	Mag. error	Ang. error
1	$\boldsymbol{V}_{LVa}$	0.351 (21.437°)	0.352 (21.254°)	-0.001	0.18°
	$\boldsymbol{V}_{LVb}$	0.75 (-80.812°)	0.752 (-80.911°)	-0.001	0.1°
	$\boldsymbol{V}_{LVc}$	0.758 (126.094°)	0.76 (125.989°)	-0.002	0.11°
	$\boldsymbol{I}_{IBRa}$	0.915 (-44.249°)	0.918 (-44.561°)	-0.003	0.31°
	$\boldsymbol{I}_{IBRb}$	0.183 (66.768°)	0.184 (68.335°)	-0.002	-1.57°
	$\boldsymbol{I}_{IBRc}$	0.866 (147.096°)	0.863 (146.794°)	0.004	0.3°
2	$\boldsymbol{V}_{LVa}$	0.802 (18.675°)	0.803 (18.527°)	-0.001	0.15°
	$\boldsymbol{V}_{LVb}$	0.797 (-89.908°)	0.798 (-90.087°)	-0.001	0.18°
	$\boldsymbol{V}_{LVc}$	0.933 (144.63°)	0.934 (144.493°)	-0.001	0.14°
	$\boldsymbol{I}_{IBRa}$	0.922 (-9.26°)	0.919 (-9.628°)	0.003	0.37°
	$\boldsymbol{I}_{IBRb}$	0.601 (-156.672°)	0.602 (-157.25°)	-0.001	0.58°
	$\boldsymbol{I}_{IBRc}$	0.527 (132.876°)	0.523 (132.318°)	0.005	0.56°

TABLE 4. Phasors of IBR3 under priority-based limiter (Scheme I).

Case	Variable	EMT	Short-circuit Model	Mag. error	Ang. error
1	$\boldsymbol{V}_{LVa}$	0.93 (31.518°)	0.932 (31.477°)	-0.002	0.04°
	$\boldsymbol{V}_{LVb}$	0.988 (-87.723°)	0.991 (-87.745°)	-0.003	0.02°
	$\boldsymbol{V}_{LVc}$	0.971 (148.949°)	0.974 (148.882°)	-0.003	0.07°
	$\boldsymbol{I}_{IBRa}$	1 (10.946°)	1 (10.395°)	0.000	0.55°
	$\boldsymbol{I}_{IBRb}$	0.943 (-103.3°)	0.942 (-103.816°)	0.001	0.52°
	$\boldsymbol{I}_{IBRc}$	1.056 (136.439°)	1.056 (135.96°)	0.000	0.48°
2	$\boldsymbol{V}_{LVa}$	0.937 (30.007°)	0.939 (29.99°)	-0.002	0.02°
	$\boldsymbol{V}_{LVb}$	0.952 (-86.849°)	0.955 (-86.833°)	-0.003	-0.02°
	$\boldsymbol{V}_{LVc}$	0.989 (150.819°)	0.992 (150.799°)	-0.003	0.02°
	$\boldsymbol{I}_{IBRa}$	1.051 (13.096°)	1.053 (12.655°)	-0.003	0.44°
	$\boldsymbol{I}_{IBRb}$	0.947 (-107.113°)	0.949 (-107.523°)	-0.002	0.41°
	$\boldsymbol{I}_{IBRc}$	1 (138.135°)	1.003 (137.727°)	-0.003	0.41°

TABLE 5. Phasors of IBR1 under 2800 limiter (Scheme II).

Case	Variable	EMT	Short-circuit Model	Mag. error	Ang. error
2	$\boldsymbol{V}_{LVa}$	0.817 (23.408°)	0.82 (23.302°)	-0.002	0.11°
	$\boldsymbol{V}_{LVb}$	0.819 (-86.257°)	0.821 (-86.364°)	-0.002	0.11°
	$\boldsymbol{V}_{LVc}$	0.942 (148.511°)	0.945 (148.398°)	-0.002	0.11°
	$\boldsymbol{I}_{IBRa}$	1.2 (3.181°)	1.2 (3.034°)	0.000	0.15°
	$\boldsymbol{I}_{IBRb}$	0.82 (-129.951°)	0.819 (-130.141°)	0.001	0.19°
	$\boldsymbol{I}_{IBRc}$	0.876 (140.087°)	0.875 (139.992°)	0.001	0.09°
3	$\boldsymbol{V}_{LVa}$	0.984 (29.606°)	0.987 (29.527°)	-0.002	0.08°
	$\boldsymbol{V}_{LVb}$	0.828 (-93.745°)	0.83 (-93.804°)	-0.001	0.06°
	$\boldsymbol{V}_{LVc}$	0.871 (157.006°)	0.873 (156.962°)	-0.002	0.04°
	$\boldsymbol{I}_{IBRa}$	0.944 (28.485°)	0.943 (28.361°)	0.001	0.12°
	$\boldsymbol{I}_{IBRb}$	1.2 (-114.944°)	1.2 (-115.181°)	0.000	0.24°
	$\boldsymbol{I}_{IBRc}$	0.715 (116.926°)	0.713 (116.612°)	0.002	0.31°

the tolerance for convergence, pre-fault conditions of IBRs, and the simplifications in IBR controllers.

To examine the performance of FRT strategies, Case 2 (Scheme I) is taken as an example. The current injection requirements specified in the IEEE 2800 standard are summarized in Appendix C. Table 8 shows the phase currents of IBR2 under different FRT strategies. With the 2800 limiter, the current in the faulty phase reaches the current limit (1.2 pu), fully utilizing the converter's current capacity. The active and reactive current contributions of IBR2 under different FRT strategies can be calculated by (1), as shown in Table 9.

With the magnitude limiter, the incremental I1R is lower than the incremental I2R, violating the IEEE 2800 standard. In addition, with these FRT strategies, I2A equals 0,

TABLE 6. Phasors of IBR2 under VI-based limiter (Scheme II).

Case	Variable	EMT	Short-circuit Model	Mag. error	Ang. error
2	$\boldsymbol{V}_{LVa}$	0.822 (25.545°)	0.828 (25.124°)	-0.006	0.42°
	$\boldsymbol{V}_{LVb}$	0.833 (-83.418°)	0.839 (-83.888°)	-0.005	0.47°
	$\boldsymbol{V}_{LVc}$	0.962 (150.529°)	0.968 (150.119°)	-0.006	0.41°
	$\boldsymbol{I}_{IBRa}$	1.199 (2.003°)	1.199 (0.528°)	0.000	1.47°
	$\boldsymbol{I}_{IBRb}$	0.792 (-132.874°)	0.799 (-134.958°)	-0.007	2.08°
	$\boldsymbol{I}_{IBRc}$	0.851 (140.764°)	0.843 (138.893°)	0.009	1.87°
3	$\boldsymbol{V}_{LVa}$	1.031 (31.438°)	1.035 (31.254°)	-0.004	0.18°
	$\boldsymbol{V}_{LVb}$	0.906 (-91.469°)	0.909 (-91.618°)	-0.003	0.15°
	$\boldsymbol{V}_{LVc}$	0.932 (156.743°)	0.936 (156.592°)	-0.004	0.15°
	$\boldsymbol{I}_{IBRa}$	0.95 (23.944°)	0.947 (23.22°)	0.002	0.72°
	$\boldsymbol{I}_{IBRb}$	1.19 (-113.511°)	1.191 (-114.266°)	0.000	0.76°
	$\boldsymbol{I}_{IBRc}$	0.808 (119.096°)	0.808 (118.157°)	0.001	0.94°

TABLE 7. Phasors of IBR1 under priority-based limiter (Scheme II).

Case	Variable	EMT	Short-circuit Model	Mag. error	Ang. error
4	$\boldsymbol{V}_{LVa}$	1.003 (27.803°)	1.006 (27.661°)	-0.003	0.14°
	$\boldsymbol{V}_{LVb}$	0.714 (-99.783°)	0.716 (-99.961°)	-0.002	0.18°
	$\boldsymbol{V}_{LVc}$	0.802 (162.937°)	0.803 (162.79°)	-0.002	0.15°
	$\boldsymbol{I}_{IBRa}$	0.77 (15.009°)	0.764 (14.339°)	0.007	0.67°
	$\boldsymbol{I}_{IBRb}$	1.187 (-130.532°)	1.186 (-131.132°)	0.000	0.6°
	$\boldsymbol{I}_{IBRc}$	0.703 (87.789°)	0.705 (86.725°)	-0.003	1.06°
5	$\boldsymbol{V}_{LVa}$	0.772 (36.581°)	0.775 (36.742°)	-0.003	-0.16°
	$\boldsymbol{V}_{LVb}$	0.771 (-83.407°)	0.775 (-83.258°)	-0.005	-0.15°
	$\boldsymbol{V}_{LVc}$	0.772 (156.683°)	0.775 (156.742°)	-0.004	-0.06°
	$\boldsymbol{I}_{IBRa}$	1.137 (1.808°)	1.138 (1.974°)	-0.001	-0.17°
	$\boldsymbol{I}_{IBRb}$	1.138 (-117.909°)	1.138 (-118.026°)	0.000	0.12°
	$\boldsymbol{I}_{IBRc}$	1.14 (122.118°)	1.138 (121.974°)	0.002	0.14°

TABLE 8. Phase currents under different current limiters.

Current limiter	$\boldsymbol{I}_{IBRa}$	$\boldsymbol{I}_{IBRb}$	$\boldsymbol{I}_{IBRc}$
Instantaneous limiter	0.917 (-9.47°)	-9.468 (0.6°)	0.597 (-157.25°)
Magnitude limiter	1.195 (7°)	6.996 (0.77°)	0.766 (-125.48°)
Priority-based limiter	1.197 (4.45°)	4.446 (0.78°)	0.779 (-129.29°)
2800 limiter	**1.2** (4.51°)	4.515 (0.78°)	0.781 (-129.18°)
VI-based limiter	1.199 (0.57°)	0.566 (0.8°)	0.799 (-134.98°)

TABLE 9. Active and reactive currents under different current limiters.

Current limiter	I^P_{IBR+}	I^Q_{IBR+}	I^P_{IBR-}	I^Q_{IBR-}	$\boldsymbol{V}_{LV+}$	$\boldsymbol{V}_{LV-}$
Instantaneous limiter	0.52	0.38	0.00	0.28	0.844 (24.241°)	0.092 (-93.923°)
Magnitude limiter	0.85	0.35	0.00	0.28	0.849 (32.297°)	0.092 (-92.716°)
Priority-based limiter	0.84	0.39	0.00	0.28	0.86 (31.594°)	0.092 (-92.802°)
2800 limiter	0.84	0.39	0.00	0.28	0.86 (31.648°)	0.092 (-92.782°)
VI-based limiter	0.81	**0.45**	0.00	0.28	**0.875** (30.454°)	0.092 (-92.952°)

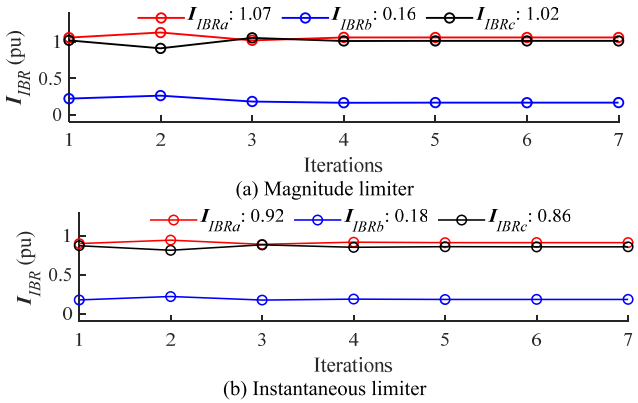

FIGURE 13. Current contribution of IBRs in Case 1 (Scheme I).

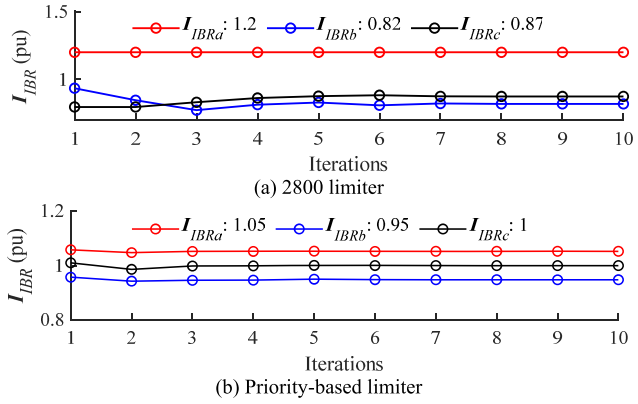

FIGURE 14. Current contribution of IBRs in Case 2 (Scheme I).

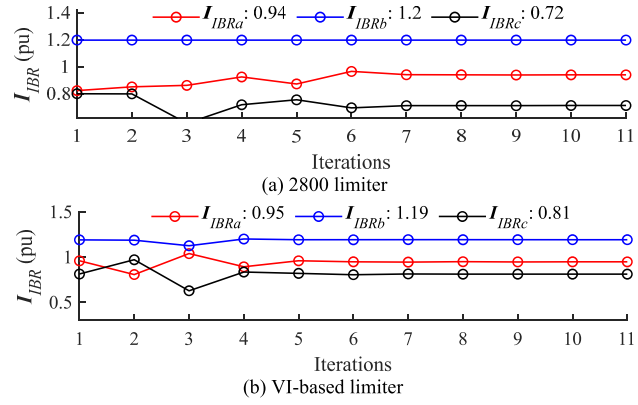

FIGURE 15. Current contribution of IBRs in Case 3 (Scheme II).

indicating that I2 leads V2 by 90°, meeting the IEEE 2800 standard. The VI-based limiter demonstrates the highest magnitude of V1, indicating that it is the most effective method for providing voltage support. Overall, following the steps of the proposed short-circuit calculation method, the system operator can efficiently perform short-circuit

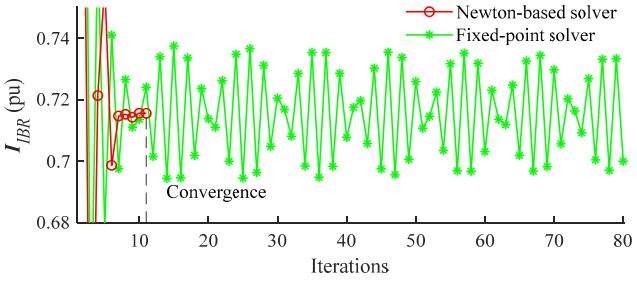

FIGURE 16. Phase C current contribution of IBR1 under different solvers (Case 3, Scheme II).

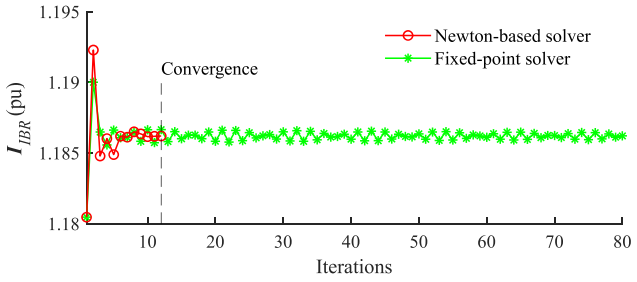

FIGURE 17. Phase B current contribution of IBR3 under different solvers (Case 4, Scheme II).

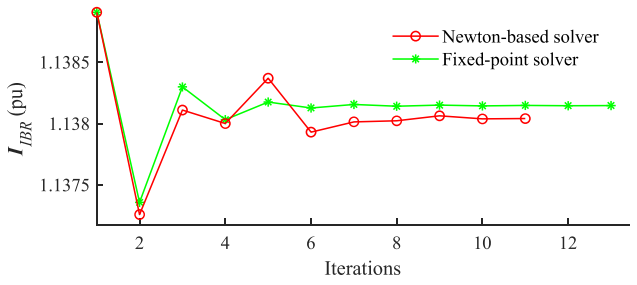

FIGURE 18. Phase B current contribution of IBR3 under different solvers (Case 5, Scheme II).

calculation of IBR-rich systems for protective relaying studies and the evaluation of FRT strategies.

C. ROBUST CONVERGENCE

The section shows that the Newton-based iterative solver shows superior convergence characteristics and addresses the non-convergence issue under the conventional fixed point-based solver. Figs. 13–15 show the iteration process. Figs. 16–18 show the comparison between the Newton-based iterative solver and the fixed-point iterative solver using MANA. Table 10 presents the iteration numbers for various scenarios.

V. CONCLUSION

Modern grid codes require IBRs to implement specific FRT strategies, which introduces complexity in current limiter design and short-circuit calculation. This paper addresses

TABLE 10. Comparison of iterations of short-circuit solvers.

Case	Number of iterations	
	Fixed-point solver	Newton-based solver
1	12	7
2	103	10
3	Non-convergence	11
4	Non-convergence	12
5	13	11

Algorithm 1 Instantaneous limiter

$\left\{I_{gsc+}^{d+lim}, I_{gsc+}^{q+lim}\right\} = \left\{k_d I_{gsc+}^{lim*}, k_q I_{gsc+}^{lim*}\right\}$;
IF $I_{gsc+}^{q+*} > I_{gsc+}^{q+lim}$
  $I_{gsc+}^{q+*} = I_{gsc+}^{q+lim}$;
ELSE IF $I_{gsc+}^{q+*} < -I_{gsc+}^{q+lim}$
  $I_{gsc+}^{q+*} = -I_{gsc+}^{q+lim}$;
  END
END
IF $I_{gsc+}^{d+*} > I_{gsc+}^{d+lim}$
  $I_{gsc+}^{d+*} = I_{gsc+}^{d+lim}$;
ELSE IF $I_{gsc+}^{d+*} < -I_{gsc+}^{d+lim}$
  $I_{gsc+}^{d+*} = -I_{gsc+}^{d+lim}$;
  END
END
$\left\{\tilde{I}_{gsc+}^{d+*}, \tilde{I}_{gsc+}^{q+*}\right\} = \left\{I_{gsc+}^{d+*}, I_{gsc+}^{q+*}\right\}$; $\tilde{\boldsymbol{I}}_{gsc+}^{*} = \left(\tilde{I}_{gsc+}^{d+*} + j\tilde{I}_{gsc+}^{q+*}\right) e^{j\theta_0}$;
RETURN $\tilde{\boldsymbol{I}}_{gsc+}^{*}$

these challenges by proposing phasor domain short-circuit models of IBRs incorporating various FRT strategies and an iterative solver for rapid short-circuit calculation in IBR-integrated power systems, combining a modified Newton algorithm with MANA formulation.

The key findings demonstrate:

(a) With the CS-based limiter, the current contribution of IBRs is determined by their FRT strategies. With the VI-based limiter, the current injection of IBRs is determined by the equivalent voltage and impedance of IBRs and AC systems.

(b) The proposed short-circuit model accurately estimates the current contribution and voltage support capability under steady-state fault conditions. The MANA formulation with Newton-based iterative solver shows superior convergence and addresses non-convergence issues when compared to the MANA formulation with fixed-point solver.

(c) From the comparative studies on these FRT strategies, the IEEE 2800 compliant limiter fully utilizes converter current capacity, and the VI-based limiter enhances the voltage support capability. The proposed short-circuit models enable protection engineers to efficiently analyze short-circuit behavior in IBR-integrated systems, support FRT strategy development, and conduct comprehensive protective relaying studies.

Algorithm 2 Magnitude limiter

$I_{gsc+}^{*} = abs(\boldsymbol{I}_{gsc+}^{dq+*})$;
IF $I_{gsc+}^{*} > I_{gsc+}^{lim}$
  $I_{gsc+}^{*} = I_{gsc+}^{lim}$;
END
$\tilde{I}_{gsc+}^{*} = I_{gsc+}^{*}$; $\tilde{\boldsymbol{I}}_{gsc+}^{*} = \tilde{I}_{gsc+}^{*} e^{j\left(\theta_0 + angle\left(I_{gsc+}^{dq+*}\right)\right)}$;
RETURN $\tilde{\boldsymbol{I}}_{gsc+}^{*}$

Algorithm 3 Priority-based limiter

IF $I_{gsc+}^{q+*} > I_{gsc+}^{lim}$
  $I_{gsc+}^{q+*} = I_{gsc+}^{lim}$;
ELSE IF $I_{gsc+}^{q+*} < -I_{gsc+}^{lim}$
  $I_{gsc+}^{q+*} = -I_{gsc+}^{lim}$;
  END
END
IF $I_{gsc+}^{d+*} > \sqrt{\left(I_{gsc+}^{lim}\right)^2 - \left(\tilde{I}_{gsc+}^{q+*}\right)^2}$
  $I_{gsc+}^{d+*} = \sqrt{\left(I_{gsc+}^{lim}\right)^2 - \left(\tilde{I}_{gsc+}^{q+*}\right)^2}$;
ELSE IF $I_{gsc+}^{d+*} < -\sqrt{\left(I_{gsc+}^{lim}\right)^2 - \left(\tilde{I}_{gsc+}^{q+*}\right)^2}$
  $I_{gsc+}^{d+*} = -\sqrt{\left(I_{gsc+}^{lim}\right)^2 - \left(\tilde{I}_{gsc+}^{q+*}\right)^2}$;
  END
END
$\left\{\tilde{I}_{gsc+}^{d+*}, \tilde{I}_{gsc+}^{q+*}\right\} = \left\{I_{gsc+}^{d+*}, I_{gsc+}^{q+*}\right\}$; $\tilde{\boldsymbol{I}}_{gsc+}^{*} = \left(\tilde{I}_{gsc+}^{d+*} + j\tilde{I}_{gsc+}^{q+*}\right) e^{j\theta_0}$;
RETURN $\tilde{\boldsymbol{I}}_{gsc+}^{*}$

APPENDIX

A. CURRENT LIMITER ALGORITHM

See Algorithms 1–5.

B. NEWTON-RAPHSON-BASED SOLVER

The Newton-Raphson-based solver [28], [29] linearizes the short-circuit model of IBRs $\tilde{\boldsymbol{I}}_{IBR} = f(\mathbf{V}_{LV})$ around the solution of the k-th iteration ($k > 1$), as given by

$$\tilde{\boldsymbol{I}}_{IBR} = \tilde{\boldsymbol{I}}_{IBR}^{(k)} + \frac{\partial f\left(\boldsymbol{V}_{LV}\right)}{\partial \boldsymbol{V}_{LV}^{(k)}}\left(\boldsymbol{V}_{LV} - \boldsymbol{V}_{LV}^{(k)}\right) \tag{A1}$$

From (A1), the IBR model can be linearized to a Norton equivalent, i.e., a virtual admittance $\boldsymbol{Y}_{IBR} = \partial f(\boldsymbol{V}_{LV}) / \partial \boldsymbol{V}_{LV}$ in parallel with an ideal current source. This added linearity allows for seamless integration of the IBR model equations with the network's linear equations. For the k-th iteration ($k > 1$), the virtual admittance can be determined as

$$\boldsymbol{Y}_{IBR}^{(k)} = -\frac{\partial f\left(\boldsymbol{V}_{LV}\right)}{\partial \boldsymbol{V}_{LV}^{(k)}} = -\frac{\tilde{\boldsymbol{I}}_{IBR}^{(k)} - \tilde{\boldsymbol{I}}_{IBR}^{(k-1)}}{\boldsymbol{V}_{LV}^{(k)} - \boldsymbol{V}_{LV}^{(k-1)}} \tag{A2}$$

Algorithm 4 IEEE 2800 compliant limiter

Calculate $\left\{I_{gsc+}^{d+*}, I_{gsc+}^{q+*}, I_{gsc-}^{d-*}, I_{gsc-}^{q-*}\right\}$ by (4) and (10);
IF $I_{gsc+}^{q+*} > I_{gsc+}^{lim}$
  $I_{gsc+}^{q+*} = I_{gsc+}^{lim}$;
ELSE IF $I_{gsc+}^{q+*} < -I_{gsc+}^{lim}$
  $I_{gsc+}^{q+*} = -I_{gsc+}^{lim}$;
  END
END
IF $I_{gsc+}^{d+*} > \sqrt{\left(I_{gsc+}^{lim}\right)^2 - \left(\tilde{I}_{gsc+}^{q+*}\right)^2}$
  $I_{gsc+}^{d+*} = \sqrt{\left(I_{gsc+}^{lim}\right)^2 - \left(\tilde{I}_{gsc+}^{q+*}\right)^2}$;
ELSE IF $I_{gsc+}^{d+*} < -\sqrt{\left(I_{gsc+}^{lim}\right)^2 - \left(\tilde{I}_{gsc+}^{q+*}\right)^2}$
  $I_{gsc+}^{d+*} = -\sqrt{\left(I_{gsc+}^{lim}\right)^2 - \left(\tilde{I}_{gsc+}^{q+*}\right)^2}$;
  END
END
$\tilde{\boldsymbol{I}}_{gsc+}^{*} = \left(I_{gsc+}^{d+*} + jI_{gsc+}^{q+*}\right) e^{j\theta_0}$;
$\tilde{\boldsymbol{I}}_{gsc-}^{*} = abs\left(\tilde{I}_{gsc-}^{d-*} + j\tilde{I}_{gsc-}^{q-*}\right) e^{j\left(\theta_0 - angle\left(\tilde{I}_{gsc-}^{d-*} + j\tilde{I}_{gsc-}^{q-*}\right)\right)}$;
$\mathbf{I}_{gsc}^{0+-*} = \left[0\ \tilde{\boldsymbol{I}}_{gsc+}^{*}\ \tilde{\boldsymbol{I}}_{gsc-}^{*}\right]$;
$\alpha = e^{j\frac{2\pi}{3}}$; $\boldsymbol{A} = \left[1\ 1\ 1;\ 1\ \alpha^2\ \alpha;\ 1\ \alpha\ \alpha^2\right]$;
$\boldsymbol{I}_{gsc}^{abc*} = \boldsymbol{A}\boldsymbol{I}_{gsc}^{0+-*}$; $K_{scale} = \frac{I_{gsc}^{lim}}{\max\left(abs\left(I_{gsc}^{abc*}\right)\right)}$;
$\tilde{\boldsymbol{I}}_{gsc+}^{*} := K_{scale}\tilde{\boldsymbol{I}}_{gsc+}^{*}$; $\tilde{\boldsymbol{I}}_{gsc-}^{*} := K_{scale}\tilde{\boldsymbol{I}}_{gsc-}^{*}$;
RETURN $\tilde{\boldsymbol{I}}_{gsc+}^{*}, \tilde{\boldsymbol{I}}_{gsc-}^{*}$

Algorithm 5 Virtual Impedance-based limiter

Assume $\boldsymbol{Z}_{vir+} = 0$, calculate $\boldsymbol{I}_{gsc+}$ by (5);
IF $abs\left(\boldsymbol{I}_{gsc+}\right) \le I_{gsc+}^{lim}$
  $R_{vir+} = 0$; $\tilde{\boldsymbol{I}}_{gsc+}^{*} = \boldsymbol{I}_{gsc+}$;
ELSE IF $abs\left(\boldsymbol{I}_{gsc+}\right) > I_{gsc+}^{lim}$
  Calculate E_{+}^{d+*} by (13);
  $R_{vir+} = abs\left(\left(\frac{E_{+}^{d+*}e^{j\theta_0} - \boldsymbol{V}_{eq+}}{I_{gsc+}^{lim}} - \boldsymbol{Z}_{eq+}\right) \Big/ (1 + j\sigma)\right)$;
  $\tilde{\boldsymbol{I}}_{gsc+}^{*} = I_{gsc+}^{lim} e^{j\left(angle\left(\frac{E_{+}^{d+*}e^{j\theta_0} - \boldsymbol{V}_{eq+}}{R_{vir+}(1+j\sigma) + \boldsymbol{Z}_{eq+}}\right)\right)}$;
  END
END
RETURN $\tilde{\boldsymbol{I}}_{gsc+}^{*}$

C. CURRENT INJECTION REQUIREMENT IN IEEE 2800 STANDARD

(a) IBRs shall be capable of injecting current up to the maximum current limit under FRT mode.

(b) For full-size-type IBR, I2 shall lead V2 by 90°−100°.

(c) During unbalanced faults, the incremental I1R shall not be lower than the incremental I2R.

TABLE 11. Detailed control parameters of IBRs.

Control strategy	Control Parameter	Value
GFM control	PSL parameter (droop control: D_P)	0.8038
	PI parameters (VI)	0.25, 65
	PI parameters (inner voltage control)	2, 200
	PI parameters (inner current control)	1, 10
GFL control	PI parameters (DDSRF-PLL)	7.5, 300
	PI parameters (DC voltage control)	1.2, 24.5
	PI parameters (inner current control)	1.6, 23.9

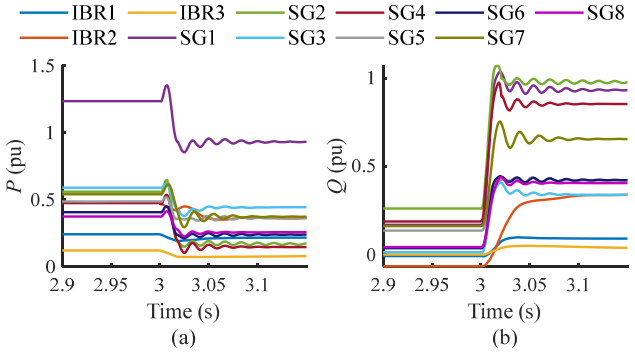

FIGURE 19. Active and reactive power outputs of generation.

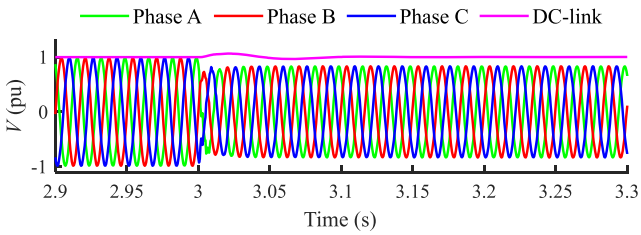

FIGURE 20. DC-link voltage and AC terminal voltage of IBR1.

D. DESCRIPTION OF THE EMPLOYED EMT MODEL

The EMT model is modified based on the EMTP benchmark and library element [13], [39], [40]. Detailed control parameters of IBRs can be found in Table 11. To examine the dynamic performance of the EMT model, a bolted ABCG fault at B14 (Scheme II) is taken as an example. The responses of the terminal voltage and active and reactive power are shown in Fig. 19 and Fig. 20. The rated power (S_{base}) is set to 1000 MVA.

REFERENCES

[1] X. Chen, Y. Chang, and I. Kocar, "Grid-forming control of DFIG-based wind turbine generator by using internal voltage vectors for asymmetrical fault ride-through," *IEEE Trans. Energy Convers.*, early access, doi: 10.1109/TEC.2024.3470588.

[2] Y. Chang, I. Kocar, J. Hu, U. Karaagac, K. W. Chan, and J. Mahseredjian, "Coordinated control of DFIG converters to comply with reactive current requirements in emerging grid codes," *J. Modern Power Syst. Clean Energy*, vol. 10, no. 2, pp. 502–514, Mar. 2022.

[3] A. Singh, V. Debusschere, N. Hadjsaid, X. Legrand, and B. Bouzigon, "Slow-interaction converter-driven stability in the distribution grid: Small-signal stability analysis with grid-following and grid-forming inverters," *IEEE Trans. Power Syst.*, vol. 39, no. 2, pp. 4521–4536, Mar. 2024.

[4] K. Strunz, K. Almunem, C. Wulkow, M. Kuschke, M. Valescudero, and X. Guillaud, "Enabling 100% renewable power systems through power electronic grid-forming converter and control: System integration for security, stability, and application to Europe," *Proc. IEEE*, vol. 111, no. 7, pp. 891–915, Jul. 2023.

[5] *IEEE Standard for Interconnection and Interoperability of Inverter-Based Resources (IBRs) Interconnecting With Associated Transmission Electric Power Systems*, Standard 2800-2022, 2022, pp. 1–180.

[6] X. Lyu and D. Groß, "Grid forming fast frequency response for PMSG-based wind turbines," *IEEE Trans. Sustain. Energy*, vol. 15, no. 1, pp. 23–38, Jan. 2024.

[7] A. Azizi and A. Hooshyar, "Fault current limiting and grid code compliance for grid-forming inverters—Part I: Problem statement," *IEEE Trans. Sustain. Energy*, vol. 15, no. 4, pp. 2486–2499, Jul. 2024.

[8] A. Haddadi, M. Zhao, I. Kocar, U. Karaagac, K. W. Chan, and E. Farantatos, "Impact of inverter-based resources on negative sequence quantities-based protection elements," *IEEE Trans. Power Deliv.*, vol. 36, no. 1, pp. 289–298, Feb. 2021.

[9] H. Geng, L. Liu, and R. Li, "Synchronization and reactive current support of PMSG-based wind farm during severe grid fault," *IEEE Trans. Sustain. Energy*, vol. 9, no. 4, pp. 1596–1604, Oct. 2018.

[10] Q. Hu, L. Fu, F. Ma, G. Wang, C. Liu, and Y. Ma, "Impact of LVRT control on transient synchronizing stability of PLL-based wind turbine converter connected to high impedance AC grid," *IEEE Trans. Power Syst.*, vol. 38, no. 6, pp. 5445–5458, Nov. 2023.

[11] G. Mayilsamy, S. R. Lee, J. H. Jeong, and Y. H. Joo, "An enhanced low-voltage ride-through for PMVG-based WTS with unified super-capacitor and rotor speed control," *IEEE J. Emerg. Sel. Topics Ind. Electron.*, vol. 6, no. 1, pp. 115–125, Jan. 2025.

[12] S. D. Tavakoli, E. Prieto-Araujo, O. Gomis-Bellmunt, and S. Galceran-Arellano, "Fault ride-through control based on voltage prioritization for grid-forming converters," *IET Renew. Power Gener.*, vol. 17, no. 6, pp. 1370–1384, Apr. 2023.

[13] U. Karaagac et al., "A generic EMT-type model for wind parks with permanent magnet synchronous generator full size converter wind turbines," *IEEE Power Energy Technol. Syst. J.*, vol. 6, pp. 131–141, 2019.

[14] B. Fan, T. Liu, F. Zhao, H. Wu, and X. Wang, "A review of current-limiting control of grid-forming inverters under symmetrical disturbances," *IEEE Open J. Power Electron.*, vol. 3, pp. 955–969, 2022.

[15] N. Baeckeland, D. Chatterjee, M. Lu, B. Johnson, and G.-S. Seo, "Overcurrent limiting in grid-forming inverters: A comprehensive review and discussion," *IEEE Trans. Power Electron.*, vol. 39, no. 11, pp. 14493–14517, Nov. 2024.

[16] N. Bottrell and T. C. Green, "Comparison of current-limiting strategies during fault ride-through of inverters to prevent latch-up and wind-up," *IEEE Trans. Power Electron.*, vol. 29, no. 7, pp. 3786–3797, Jul. 2014.

[17] M. A. Zamani, A. Yazdani, and T. S. Sidhu, "A control strategy for enhanced operation of inverter-based microgrids under transient disturbances and network faults," *IEEE Trans. Power Del.*, vol. 27, no. 4, pp. 1737–1747, Oct. 2012.

[18] K. G. Saffar, S. Driss, and F. B. Ajaei, "Impacts of current limiting on the transient stability of the virtual synchronous generator," *IEEE Trans. Power Electron.*, vol. 38, no. 2, pp. 1509–1521, Feb. 2023.

[19] A. D. Paquette and D. M. Divan, "Virtual impedance current limiting for inverters in microgrids with synchronous generators," *IEEE Trans. Ind. Appl.*, vol. 51, no. 2, pp. 1630–1638, Mar. 2015.

[20] A. Azizi and A. Hooshyar, "Fault current limiting and grid code compliance for grid-forming inverters—Part II: Solution," *IEEE Trans. Sustain. Energy*, vol. 15, no. 4, pp. 2500–2517, Oct. 2024.

[21] M.-A. Nasr and A. Hooshyar, "Controlling grid-forming inverters to meet the negative-sequence current requirements of the IEEE Standard 2800–2022," *IEEE Trans. Power Del.*, vol. 38, no. 4, pp. 2541–2555, Aug. 2023.

[22] MathWorks Simscape Team (2024). *Renewable Energy Integration Design With Simscape*. GitHub. [Online]. Available: https://github.com/simscape/Renewable-Energy-Integration-Simscape/releases/tag/23.2.1.20

[23] T. Kauffmann, U. Karaagac, I. Kocar, S. Jensen, J. Mahseredjian, and E. Farantatos, "An accurate type III wind turbine generator short circuit model for protection applications," *IEEE Trans. Power Del.*, vol. 32, no. 6, pp. 2370–2379, Dec. 2017.

[24] Y. Chang, I. Kocar, E. Farantatos, A. Haddadi, and M. Patel, "Short-circuit modeling of DFIG-based wtg in sequence domain considering various fault-ride-through requirements and solutions," *IEEE Trans. Power Del.*, vol. 38, no. 3, pp. 2088–2100, Jun. 2023.

[25] T. Kauffmann et al., "Short-circuit model for type-IV wind turbine generators with decoupled sequence control," *IEEE Trans. Power Del.*, vol. 34, no. 5, pp. 1998–2007, Oct. 2019.

[26] J.-S. Lacroix, "Multiphase short-circuit analysis solver in phase domain using a modified-augmented-nodal analysis approach," Ph.D. dissertation, Département De Génie ÉLectrique, PolyPublie, École Polytechnique de Montréal, Montreal, QC, Canada, 2012.

[27] I. Kocar, J. Mahseredjian, U. Karaagac, G. Soykan, and O. Saad, "Multiphase load-flow solution for large-scale distribution systems using MANA," *IEEE Trans. Power Del.*, vol. 29, no. 2, pp. 908–915, Apr. 2014.

[28] A. Haddadi, E. Farantatos, and I. Kocar, "A robust solver for phasor-domain short-circuit analysis with inverter-based resources," 2024, *arXiv:2411.12006*.

[29] *Inverter Based Resource Short-Circuit Modeling-2024 Research Summary*. EPRI, Palo Alto, CA, USA, 2024.

[30] S. Favuzza, R. Musca, G. Zizzo, and J. A. Sa'ed, "Comparative modeling and analysis of EMT and phasor RMS grid-forming converters under different power system dynamics," *IEEE Trans. Ind. Appl.*, vol. 60, no. 2, pp. 3613–3624, Apr. 2024.

[31] C. Fang, L. Mu, Z. Wang, and G. Chen, "Analysis of grid-forming IIDG's transient- and steady-state fault model," *IEEE Trans. Smart Grid*, vol. 13, no. 2, pp. 1187–1199, Mar. 2022.

[32] V. C. Cunha et al., "Generalized formulation of steady-state equivalent circuit models of grid-forming inverters," *IEEE Open Access J. Power Energy*, vol. 8, pp. 352–364, 2021.

[33] R. C. Dugan and T. E. McDermott, "An open source platform for collaborating on smart grid research," in *Proc. IEEE Power Energy Soc. Gen. Meeting*, Jul. 2011, pp. 1–7.

[34] W. Du et al., "Positive-sequence modeling of droop-controlled grid-forming inverters for transient stability simulation of transmission systems," *IEEE Trans. Power Del.*, vol. 39, no. 3, pp. 1736–1748, Jun. 2024.

[35] Z. Chen, H. Liu, P. J. Hart, W. Du, F. Tuffner, and U. C. Nwaneto, "Per-phase phasor modeling of GFL and GFM inverters for distribution system dynamic studies," in *Proc. IEEE Power Energy Soc. Innov. Smart Grid Technol. Conf. (ISGT)*, Feb. 2024, pp. 1–5.

[36] *Technical Requirements for the Connection and Operation of Customer Installations To the High-voltage Network (TCChigh-Voltage)*, document VDE, VDE-AR-N 4120, 2015.

[37] W. Wes Baker, M. Patel, A. Haddadi, E. Farantatos, and J. C. Boemer, "Inverter current limit logic based on the IEEE 2800-2022 unbalanced fault response requirements," presented at the IEEE Power Energy Soc. Gen. Meeting (PESGM), Jul. 2023.

[38] I. Kocar, J.-S. Lacroix, and F. Therrien, "General and simplified computation of fault flow and contribution of distributed sources in unbalanced distribution networks," in *Proc. IEEE Power Energy Soc. Gen. Meeting*, San Diego, CA, USA, Jul. 2012, pp. 1–8.

[39] L. Gérin-Lajoie, *IEEE PES Task Force on Benchmark Systems for Stability Controls*, document EMTP-RV 39-Bus System, Version 1.5, Mar. 2015.

[40] A. Haddadi et al., "Power system test cases for EMT-type simulation studies," *CIGRE Tech. Brochure*, vol. 736, pp. 1–142, Aug. 2018.

XINQUAN CHEN (Graduate Student Member, IEEE) received the B.Eng. and M.Sc. degrees in electrical engineering from South China University of Technology, Guangzhou, China, in 2018 and 2021, respectively. He is currently pursuing the Ph.D. degree with the Department of Electrical and Electronic Engineering, The Hong Kong Polytechnic University. His research interests include power system dynamics and protection, inverter control, renewable energy sources, and HVDC technology.

ABOUTALEB HADDADI (Senior Member, IEEE) received the Ph.D. degree in electrical and computer engineering from McGill University, Montreal, QC, Canada, in 2015. From 2015 to 2020, he was a Post-Doctoral Fellow and a Research Associate with the Polytechnique Montréal, Montréal. Since 2020, he has been with the Electric Power Research Institute, Palo Alto, CA, USA, as a Senior Engineer/Scientist and the Technical Lead/Project Manager, where he leads research and development activities related to bulk system and distributed renewable energy resources modeling and system integration impacts. He is also the EPRI Manager of the Advanced Grid Innovation Laboratory for Energy, New York Power Authority, White Plains, NY, USA. He is also the Chair of CIGRE working group C4.60 and is further active in a number of working groups of IEEE Power and Energy Society, Western Electricity Coordinating Council, and North American Electric Reliability Corporation. His research interests include renewable resource integration, power system protection, and power system modeling and simulation.

ZHE YANG (Member, IEEE) was born in China, in 1994. He received the bachelor's degree in electrical engineering from Northeast Electric Power University, Jilin, China, in 2017, the master's degree in electrical engineering from North China Electric Power University, Beijing, China, in 2020, and the Ph.D. degree in energy technology in AAU energy from Aalborg University, Aalborg, Denmark, in 2023. Currently, he is an UKRI Fellow with the Department of Electrical and Electronic Engineering, Imperial College London, London, U.K. His research interests include short circuit modeling, fault-ride-through strategies, and protection technologies for renewable energy systems.

EVANGELOS FARANTATOS (Senior Member, IEEE) received the Diploma degree in electrical and computer engineering from the National Technical University of Athens, Athens, Greece, in 2006, and the M.S. and Ph.D. degrees from Georgia Institute of Technology, Atlanta, GA, USA, in 2009 and 2012, respectively. He is currently a Principal Project Manager with the Grid Operations and Planning R&D Group, EPRI, Palo Alto, CA, USA. He is managing and leading the technical work of various research and development projects related to synchrophasor technology, power systems monitoring and control, power systems stability and dynamics, renewable energy resources modeling, and grid operation with high levels of inverter-based resources and system protection. In Summer 2009, he was an Intern with MISO.

ILHAN KOCAR (Senior Member, IEEE) received the B.Sc. and M.Sc. degrees in EEE from Orta Doğu Teknik Üniversitesi, Ankara, Türkiye, in 1998 and 2003, respectively, and the Ph.D. degree in EE from the École Polytechnique de Montréal (affiliated with Université de Montréal), QC, Canada, in 2009. He has 25 years of diverse experience in the power engineering field across industry, academia, and major regions, including North America, Asia, and Europe. He is a Full Professor at Polytechnique Montréal and President of DIgSILENT North America Inc. His research aims to address critical challenges in integrating renewable energy sources into power systems. He is an Editor of IEEE TRANSACTIONS ON POWER DELIVERY.